Wind and Structures, *Vol. 30, No. 5 (2020) 465-474*
DOI: https://doi.org/10.12989/was.2020.30.5.465

DNS of vortex-induced vibrations of a yawed flexible cylinder near a plane boundary

Zhimeng Zhang[1a], Chunning Ji*[1b], Md. Mahbub Alam[2c] and Dong Xu[1d]

[1]State Key Laboratory of Hydraulic Engineering Simulation & Safety, Tianjin University, Tianjin, 300072, China.
[2]Institute for Turbulence-Noise-Vibration Interaction and Control, Harbin Institute of Technology (Shenzhen), Shenzhen 518055, China

(Received November 4, 2019, Revised December 27, 2019, Accepted March 1, 2020)

Abstract. Vortex-induced vibrations of a yawed flexible cylinder near a plane boundary are numerically investigated at a Reynolds number Re_n = 500 based on normal component of freestream velocity. Free to oscillate in the in-line and cross-flow directions, the cylinder with an aspect ratio of 25 is pinned-pinned at both ends at a fixed wall-cylinder gap ratio G/D = 0.8, where D is the cylinder diameter. The cylinder yaw angle (α) is varied from 0° to 60° with an increment of 15°. The main focus is given on the influence of α on structural vibrations, flow patterns, hydrodynamic forces, and IP (Independence Principle) validity. The vortex shedding pattern, contingent on α, is parallel at α=0°, negatively-yawed at $\alpha \leq 15°$ and positively-yawed at $\alpha \geq 30°$. In the negatively- and positively-yawed vortex shedding patterns, the inclination direction of the spanwise vortex rows is in the opposite and same directions of α, respectively. Both in-line and cross-flow vibration amplitudes are symmetric to the midspan, regardless of α. The RMS lift coefficient $C_{L,rms}$ exhibits asymmetry along the span when $\alpha \neq 0°$, maximum $C_{L,rms}$ occurring on the lower and upper halves of the cylinder for negatively- and positively-yawed vortex shedding patterns, respectively. The IP is well followed in predicting the vibration amplitudes and drag forces for $\alpha \leq 45°$ while invalid in predicting lift forces for $\alpha \geq 30°$. The vortex-shedding frequency and the vibration frequency are well predicted for α = 0° - 60° examined.

Keywords: yawed flexible cylinder; direct numerical simulation; Independence Principle; vortex-shedding pattern

1. Introduction

Vortex-induced vibration (VIV) of a flexible circular cylinder is widely encountered in engineering areas especially in offshore applications, such as subsea cables and pipelines. The VIV of these slender bodies exposed to ocean currents aggravates their fatigue damage. In practical applications, the flexible structures are not always perpendicular to the oncoming flow direction but are often inclined. The former is widely examined because of its simplicity while the latter is scarcely reported although representing the most general case in engineering applications.

The proximity of a plane boundary induces complex interaction between the wall boundary layer and the cylinder shear layers, which significantly affects the flow field around the cylinder. The vital parameters influencing the interaction are the Reynolds number (Re), boundary layer thickness (δ/D), gap ratio (G/D), and cylinder yaw angle (α), where Re is based on the freestream approaching velocity U and cylinder diameter D, and G is the distance between the lower surface of the cylinder and the wall. Here, the α is defined as the angle between the oncoming flow direction and the cylinder cross-sectional plane, i.e., the α = 0° corresponding to the freestream velocity normal to the cylinder axis (Hsieh *et al*. 2016, Younis *et al*. 2016, He *et al*. 2017, Zang and Zhou 2017, Bai and Alam 2018, Derakhshandeh and Alam 2018, 2019a, 2019b, Ji *et al*. 2019). For a fixed cylinder (α=0°) near a plane boundary, Bearman and Zdravkovich (1978) and Lei *et al*. (1999) reported that the vortex shedding was suppressed for 0.2 < G/D < 0.3 irrespective of G/D = 0.0 - 3.0 examined. At a small G/D, the vorticity of the gap-side vortex from the cylinder was offset by the reverse vorticity of the boundary layer flow; the gap-side shear layer of the cylinder thus lost the strength of shedding vortices. Based on the wake patterns at different G/D in Wang and Tan (2008a, 2008b) and He *et al*. (2017), four flow regimes were recognized, i.e., (i) $0 \leq G/D < 0.3$, the gap-side vortex-shedding of the cylinder was weak or completely suppressed; (ii) $0.3 < G/D < 1.0$, the cylinder gap-side shear layer and the wall boundary layer detached from the wall formed counterclockwise and clockwise vortices, respectively. Strong interactions existed between the vortices and the freestream-side vortex of the cylinder; (iii) $1.0 < G/D \leq 2.0$, periodic vortex shedding appeared on both sides of the cylinder while the recirculation length of the boundary layer decreased owing to the weakening interaction with the gap-side vortices; and (iv) G/D >2.0, the wake of the cylinder was similar to that of an isolated one. Similar results were

*Corresponding author, Ph. D. Professor
E-mail: cnji@tju.edu.cn
[a]Ph.D. Student
[b]Professor
[c]Professor
[d]Associate Professor

ISSN: 1226-6116 (Print), 1598-6225 (Online)

also found in the numerical simulations of flows around a circular cylinder at different Re_n and G/D in Sarkar and Sarkar (2010) and Yoon *et al*. (2010). Lei and Cheng (2000) studied fluid forces on a near-wall cylinder at Re = 80 ~ 1000 and showed that the maximum and RMS (root-mean-square) of the lift coefficient and vortex intensity decreased with decreasing G/D and Re.

For the VIV of a near-wall elastically supported rigid cylinder with α = 0°, Tham *et al*. (2015) and Li *et al*. (2016) showed that both in-line and crossflow vibrations were significantly influenced by the wall. For 1-DOF (degree-of-freedom) VIV, both vibration amplitude and lift force were increased compared with those of an isolated cylinder. For 2-DOF VIV, the in-line vibration amplitude increased, whereas the vibration frequency decreased, with obvious beating responses when the cylinder response entering and leaving the lock-in region. However, the wall proximity did not significantly alter the cross-flow response. Hsieh *et al*. (2016) performed an experimental study on the VIV of a near-wall cylinder at G/D = 0.8. The vibration and vortex-shedding frequencies were identical in the lock-in region, and the corresponding vortex shedding pattern was 2S (two single vortices shed in one oscillation cycle). Wang *et al*. (2013) stated that the cylinder still vibrated even at a very small G/D (= 0.05) while periodic vortex shedding was found only at the freestream side of the cylinder, forming a single vortex street in the wake. Different from the fixed cylinder counterpart, the three regimes of G/D were identified for a near-wall vibrating cylinder, i.e., (i) the vortex-shedding-suppression regime (G/D < 0.3), where vortices periodically shed from the freestream side, forming a one-sided vortex street in the wake; (ii) the intermediate regime (0.3 ≤ G/D <1.0), where the wall effect was significant, resulting in an asymmetric vortex-shedding; and (iii) the wall-effect-free regime (G/D ≥1.0), where the wake resembled that of an isolated cylinder.

The influence of α on the flow around a cylinder, either stationary or vibrating, was documented in the literature (e.g., Alam and Zhou 2007, Zhou *et al*. 2010, Franzini *et al*. 2013, and Zhao *et al*. 2013). For a stationary cylinder with a large α, the spanwise vortex rows were yawed with respect to the cylinder axis, and the vortex-shedding yaw angle was smaller than the cylinder yaw angle. However, for a vibrating rigid cylinder, the yaw angle of the spanwise vortex rows was smaller than that for the stationary cylinder. Moreover, the vortex rows in the wake were parallel to the cylinder axis approximately when the vibration amplitude was large enough.

To predict the hydrodynamics of an inclined cylinder, the IP (Independent Principle) is widely applied. It assumes that the hydrodynamics is only driven by the normal component U_n of U while the tangential component aligned with the cylinder axis has a negligible effect. According to the criteria suggested by Zhou *et al*. (2010), Franzini *et al*. (2013), and Zhao *et al*. (2013), the IP is valid when the relative difference of the hydrodynamics is smaller than 15% between an inclined cylinder (reference velocity U_n) and a normal cylinder. Although no consensus exists regarding the range of the IP validity, it is generally accepted that the IP can provide accurate predictions of the fluid forces at α < 45° for an isolated cylinder, and the relative error increases with the increasing α (Alam and Zhou 2007, Zhou *et al*. 2010, Franzini *et al*. 2013, Zhao *et al*. 2013). Bourguet *et al*. (2015) numerically investigated the VIV of a flexible cylinder at α = 60° and Re=500. In the case of a high-tension configuration where the in-line bending of the cylinder was small, the IP at this large α is still valid in predicting the vibration responses and fluid forces. However, in the lower-tension case corresponding to a large in-line bending, unacceptable errors existed in the IP prediction. A similar study at α = 80° (Bourguet and Triantafyllou 2014) showed that the structural vibrations and hydrodynamic forces were asymmetric in the spanwise direction, making the IP invalid.

Zhao *et al*. (2009) and Thapa *et al*. (2014) reported a much more complex flow-cylinder interaction with the proximity of a wall. The three-dimensionality of the wake was undermined with an increase in α while the degree of vortex shedding suppression was increased. However, in the numerical study of Ji *et al*. (2019), the wake three-dimensionality was intensified with increasing α. The IP was valid in predicting the hydrodynamic forces and wake patterns when α ≤ 15°, producing unacceptable errors when α ≥ 30°. In the experimental studies on VIV of a flexible cylinder at Re=800-16000, Han *et al*. (2017) and Xu *et al*. (2018) found that the IP was valid for predicting the multi-mode responses when α ≤ 30°. Zang and Zhou (2017) experimentally studied the transverse VIV of an elastically mounted rigid cylinder near a plane boundary at different α and G/D. The results showed that both vibration amplitude and frequency increased with decreasing G/D, and the IP is valid at α ≤ 30° and G/D ≥ 0.8.

To the best of the authors' knowledge, studies on the VIV of a flexible cylinder near a flat wall at different yaw angles are scarce. In the present study, the 2-DOF VIV of a yawed flexible cylinder close to a plane boundary is investigated by performing three-dimensional direct numerical simulations (DNS) at G/D = 0.8 and 0° ≤ α ≤ 60°. The normal Reynolds number Re_n (reference velocity U_n) is kept constant at 500. The vibration responses, wake patterns, fluid forces and the validity of the IP are analyzed and presented.

2. Numerical methodology

2.1 Numerical method and validation

The fluid-structure interaction (FSI) is simulated by using the immersed boundary (IB) method. An extra body force is added into the momentum equation to manifest the interaction between fluid and structure. The conservative form of the second-order Adams-Bashforth temporal-discretized governing equations of incompressible fluid flow using the IB method are

$$\mathbf{u}^{n+1} = \mathbf{u}^n + \delta t\left(\tfrac{3}{2}\mathbf{h}^n - \tfrac{1}{2}\mathbf{h}^{n-1} - \tfrac{3}{2}\nabla p^n + \tfrac{1}{2}\nabla p^{n-1}\right) + \mathbf{f}^{n+\frac{1}{2}}\delta t \quad (1)$$

$$\nabla \cdot \mathbf{u}^{n+1} = 0 \quad (2)$$

where, $\mathbf{u}$ is the velocity, p is the pressure, $\mathbf{h}$= $\nabla\cdot(-\mathbf{uu} + \nu(\nabla\mathbf{u}+\nabla\mathbf{u}^{\mathrm{T}}))$ comprises of the convective and diffusive terms, ∇ denotes gradient operator, ν is the kinematic viscosity of the fluid, superscript T is matrix transposition, and superscript n+1, n+1/2, n, n-1 indicate the time step. **f** denotes the extra body force and is calculated as

$$\mathbf{f}^{n+\frac{1}{2}}\delta t = D\left(\mathbf{F}^{n+\frac{1}{2}}\right)\delta t = D\left(\mathbf{V}^{n+1} - I\left(\mathbf{u}^{n} + \delta t\left(\tfrac{3}{2}\mathbf{h}^{n} - \tfrac{1}{2}\mathbf{h}^{n-1} - \tfrac{3}{2}\nabla p^{n} + \tfrac{1}{2}\nabla p^{n-1}\right)\right)\right) \quad (3)$$

where, **F** is the extra body force on the IB points, **V** is the desired velocity of the IB points obtained by solving the governing equation of cylinder motion, $I(\varphi, \mathbf{X}_i)$ and $D(\Phi,x)$ are the interpolation and distribution functions suggested by Peskin (1972), respectively.

The two-step predictor-corrector procedure is adopted for the decoupling of the flow governing equations (Eqs. (1) - (3)). The resultant pressure Poisson equation is solved by using the biconjugate gradient stabilized method, preconditioned by using the geometric multi-grid method. For the sake of conciseness, details of the methodology are not presented here and readers can refer to our previous work (Chen *et al.* 2019a, 2019b, Ji *et al.* 2012, 2019a, 2019b) for further information.

The flexible cylinder is modeled as a pinned-pinned Euler-Bernoulli beam, mimicking the submarine pipeline in reality, and free to oscillate in the in-line (x-axis) and cross-flow (y-axis) directions, as shown in Fig. 1. The aspect ratio of the cylinder is L/D =25, where L denotes the spanwise length. The cylinder mass ratio is $m^* = 4\overline{m}/(\pi\rho_f D^2) = 8.9$, where $\overline{m}$ is the cylinder mass per unit length and ρ_f is the fluid density. The non-dimensional governing equation for the structural dynamics can be expressed as follows

$$\overline{m}\ddot{\zeta}_{(x,y)} + EI\zeta^{4}_{(x,y)} = F_{(x,y)} \quad (4)$$

where the superscripts '··' and '4' denote the second temporal and fourth-order spatial derivatives, respectively. The $\zeta_{(x,y)}$ is the displacement, $F_{(x,y)}$ is the hydrodynamic force, and EI is the bending stiffness. The structural damping is set to zero to enhance vibration amplitude.

To verify the accuracy of the numerical methodology, the flow around an isolated cylinder at Re = 500 is simulated. Table 1 compares the time-mean drag coefficient $\overline{C}_D$, fluctuating (r.m.s.) lift coefficient $C_{L,rms}$, Strouhal number St, base pressure coefficient C_{pb}, and the normalized spanwise vortex wavelength λ_z/D between the present and published results. A good agreement is achieved, suggesting that the accuracy of the numerical methodology is acceptable.

Table 1 Comparison of hydrodynamic parameters for an isolated cylinder at Re = 500

	$\overline{C}_D$	$C_{L,rms}$	St	$-C_{pb}$	λ_z/D
Present	1.162	0.283	0.207	0.928	0.96
Zhao *et al.* (2013)	1.225	0.388	0.208	--	--
Bourguet and Triantafyllou (2014)	1.141	--	0.208	--	--
Jiang and Cheng (2017)	--	--	0.206	0.967 (Re=400)	--
Williamson (2003)	--	--	--	0.901	0.91
Williamson and Roshko (1990)	--	--	--	0.902	--
Mittal and Balachandar (1995)	--	--	--	0.918	--
Wu *et al.* (1994)	--	--	--	--	0.85
Mansy *et al.* (1994)	--	--	--	--	≈1.0

2.2 Simulation parameters

In present study, the normal Reynolds number, defined as $Re_n = U_nD/\nu$, is set to 500. The reduced velocity is set to as $U_r = U_n/f_1D = 4.9$, where $f_1 = \frac{1}{2\pi}(\frac{i\pi}{L})^2\sqrt{\frac{EI}{\overline{m}}}$ (i = 1) is the 1st mode natural frequency of the cylinder and U_n is the normal inflow velocity at 1D above the plane boundary. The gap between the cylinder and wall is fixed at G/D = 0.8 lying the intermediate regime (0.3 ≤ G/D <1.0) where the proximity of the plane boundary has a significant influence on the wake pattern (Wang *et al.* 2013). The cylinder is horizontally placed above the wall.

Details of the computational domain and the boundary conditions are presented in Fig. 1(a). The coordinate origin is pinpointed on a side wall, 6D downstream the cylinder center and 3D above the bottom wall. The cylinder axis is parallel to the z-axis, passing through [-6D, -1.7D] on the x-y plane. The computational domain is a rectangular box Ω = [-21D, 39D] × [-3D, 37D] × [0, 25D] discretized by using a Cartesian mesh with a resolution of 768×384×256 (streamwise × transverse × spanwise). A uniform mesh with a grid spacing of $\Delta x = \Delta y = D/32$ is adopted in a rectangular region of [-8D,8D] × [-3D,3D] around the cylinder in the x-y plane to ensure the high simulation accuracy. Outside this region, a stretched mesh is used to keep the total grids number within an affordable range. Along the cylinder axis, 256 planes are adopted with a spanwise grid spacing of $\Delta z \approx 0.1D$. The Dirichlet boundary conditions and the Neumann boundary conditions are imposed at the inflow and outflow, respectively. The top boundary is set as a free-slip wall while the bottom boundary and the cylinder surface are set as no-slip walls. Periodicity is imposed in the spanwise direction.

A mean velocity profile (Thapa *et al.* 2014) is adopted at the inlet and defined as

$$(u, v, w) = (U\cos\alpha, 0, U\sin\alpha) \quad (5)$$

where U is the velocity profile given by

$$\frac{U}{u_\tau} = \begin{cases} \dfrac{yu_\tau}{\nu}, & \text{when } \dfrac{yu_\tau}{\nu} \le 11.63 \\ \dfrac{1}{k}\ln(9.0\dfrac{yu_\tau}{\nu}), & \text{when } \dfrac{yu_\tau}{\nu} > 11.63 \end{cases} \quad (6)$$

where y is the height from the bottom wall, u_τ is the friction velocity, and k = 0.4 is the von Kármán constant. The

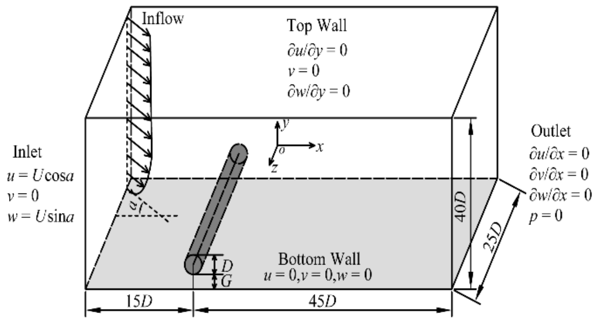

(a) Computational domain and boundary conditions

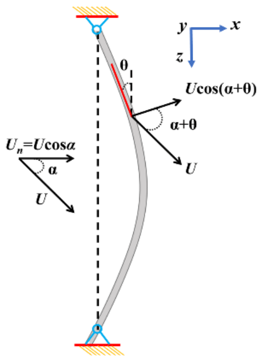

(b) Sketch of the physical configuration (plan view)

Fig. 1 Computational domain, boundary conditions and sketch of the physical configuration. The initial position of the flexible cylinder is indicated by a dashed black line

yu_τ/ν = 11.63 refers to the boundary between the viscous sublayer and the logarithmic region (Thapa *et al*. 2014).

3. Numerical results and discussion

3.1 Vortex shedding pattern

Fig. 2 shows the instantaneous vortex-shedding pattern downstream of the cylinder when the cylinder vibration is statistically stable and the wake is fully developed. It can be seen that three distinct wake patterns are observed at different α, i.e. parallel vortex shedding pattern at α = 0°, negatively-yawed vortex shedding pattern at α = 15° and positively-yawed vortex shedding pattern at α ≥ 30°.

At α = 0°, although the spanwise vortex rows downstream of the cylinder are significantly distorted due to the streamwise vortex filaments, they are essentially parallel to the cylinder axis, indicating the synchronized vortex shedding at different spanwise positions. As the vortex shedding (blue) from the gap side of the cylinder weakens, the vortices (red) shed from the freestream side materialize in the wake. Note that the spanwise vortex rows appear being more twisted and disordered as farther away from the cylinder. A large number of streamwise vortex filaments appear connecting the adjacent spanwise vortex rows, and the mean spanwise distance between the streamwise filaments is approximately 1*D*, signifying the development of mode B (Williamson 1996, Bai and Alam 2018).

At α = 15°, the vortex shedding is yawed in the opposite direction to the cylinder yaw angle, hence the shedding is named as negatively-yawed vortex shedding. The vortex shedding is not parallel, i.e., the vortex-shedding along the span is not synchronized. At α ≥ 30°, the spanwise vortex rows are yawed in the same direction of α, opposite to that at α = 15°. We, therefore, refer this pattern as positively-yawed vortex shedding pattern. For example, at α = 60° (Fig. 2(e)), the spanwise vortex row near the cylinder is yawed with respect to the cylinder axis, and its orientation is the same as that of the oncoming flow. The streamwise distance between the spanwise vortex row and cylinder increases gradually with the increasing *z*, which shows that the phase of vortex shedding, and thus the lift, varies along the span. Compared with the cases of small yaw angles (α ≤ 15°), the spanwise vortex rows downstream are more distorted and the streamwise vortex filaments are denser and stronger, leading to a further enhanced three-dimensionality of the wake. This contradicts the observation of Thapa *et al.* (2014) and Zhao *et al.* (2013) for a fixed cylinder in the vicinity of a wall that the degree of three-dimensionality of the wake diminishes with the increasing α. The discrepancy can be attributed to that in present study the normal Reynolds number (Re_n = 500) remains unchanged with α, whereas in Thapa *et al.* (2014) and Zhao *et al.* (2013) the Reynolds number based on the resultant inflow velocity is unchanged and Re_n decreases with the increasing α. Therefore, the intensified three-dimensionality of the wake is related to the higher Re_n in this study.

The flow past the vibrating cylinder at the yaw angle α = 15° and 45° is visualized in Fig. 3 by showing the instantaneous iso-surfaces of λ_2 = -1.0. Results for a stationary cylinder at α = 45° are also presented to see how the cylinder vibration impacts on the wake structure. It is seen from Fig. 3(a), 3(b) that the spanwise vortex rows are highly twisted, with vortex splitting and coalescence in the wake. The vortex rows exhibit different oblique angles β, depending on α, i.e., β ≈ -5° when α = 15° (Fig. 3(a)), and β ≈ 30° when α = 45° (Fig. 3(b)). However, for the stationary cylinder, the spanwise vortex rows appear to be fairly linear, with β ≈ -17°.

The most striking feature shown in Fig. 3(a) - 3(c) is the different signs of the orientation angles of the spanwise vortex rows shed from the vibrating and stationary cylinders. In the stationary case (Fig. 3(c)), the oblique direction of the slant vortex rows is opposite to that of the oncoming flow, consistent with the observation in Bourguet *et al.* (2015) and Bourguet and Triantafyllou (2014). However, in the vibrating case (Fig. 3(a-b)), the oblique direction of the vortex rows is opposite to that of the cylinder at α = 15°, but is the same as that of the cylinder for α ≥ 30°. Moreover, the spanwise vortex rows are approximately parallel to each other in the stationary case. However, in the vibrating case, the spanwise vortex rows wavy and the spacing between two adjacent rows varies along the span. This is inconsistent with the observation of Ramberg (1983) for a wall-free cylinder that the transverse oscillation of a cylinder tends to force parallel vortex shedding. All these discrepancies can be attributed to the proximity of the flat wall and the induced complex cylinder-wake interaction.

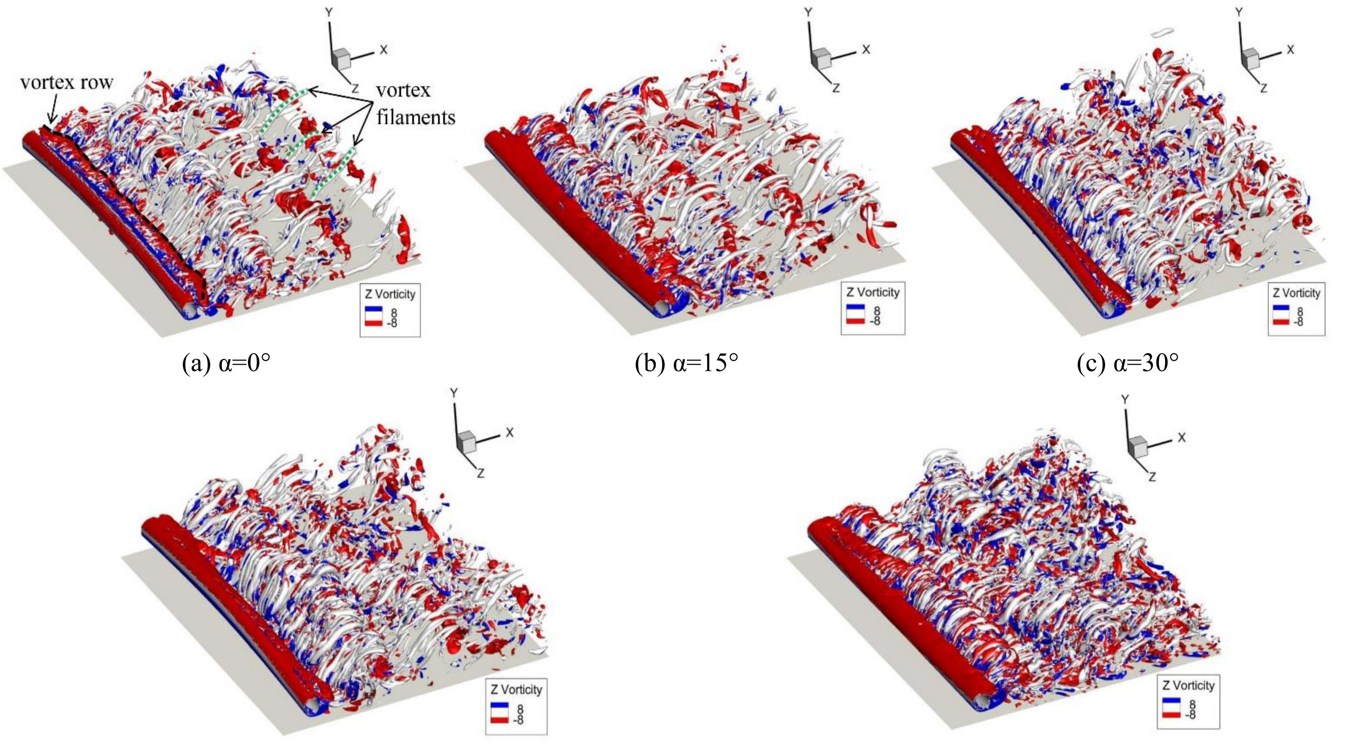

(a) α=0° (b) α=15° (c) α=30°

(d) α=45° (e) α=60°

Fig. 2 Dependence of vortex-shedding pattern on α. Vortices are visualized by using iso-surfaces of non-dimensional λ_2 (= -1.0) (Jeong and Hussain 1995) - the second largest eigenvalue of the symmetric tensor $\mathbf{S}^2+\mathbf{\Omega}^2$, where $\mathbf{S}$ and $\mathbf{\Omega}$ are the symmetric and asymmetric parts of the velocity gradient tensor $\nabla\mathbf{u}$, respectively. The color on the iso-surfaces indicates the spanwise vorticity. The dashed black lines and the dotted green lines in (a) represent the spanwise vortex rows and streamwise vortex filaments, respectively

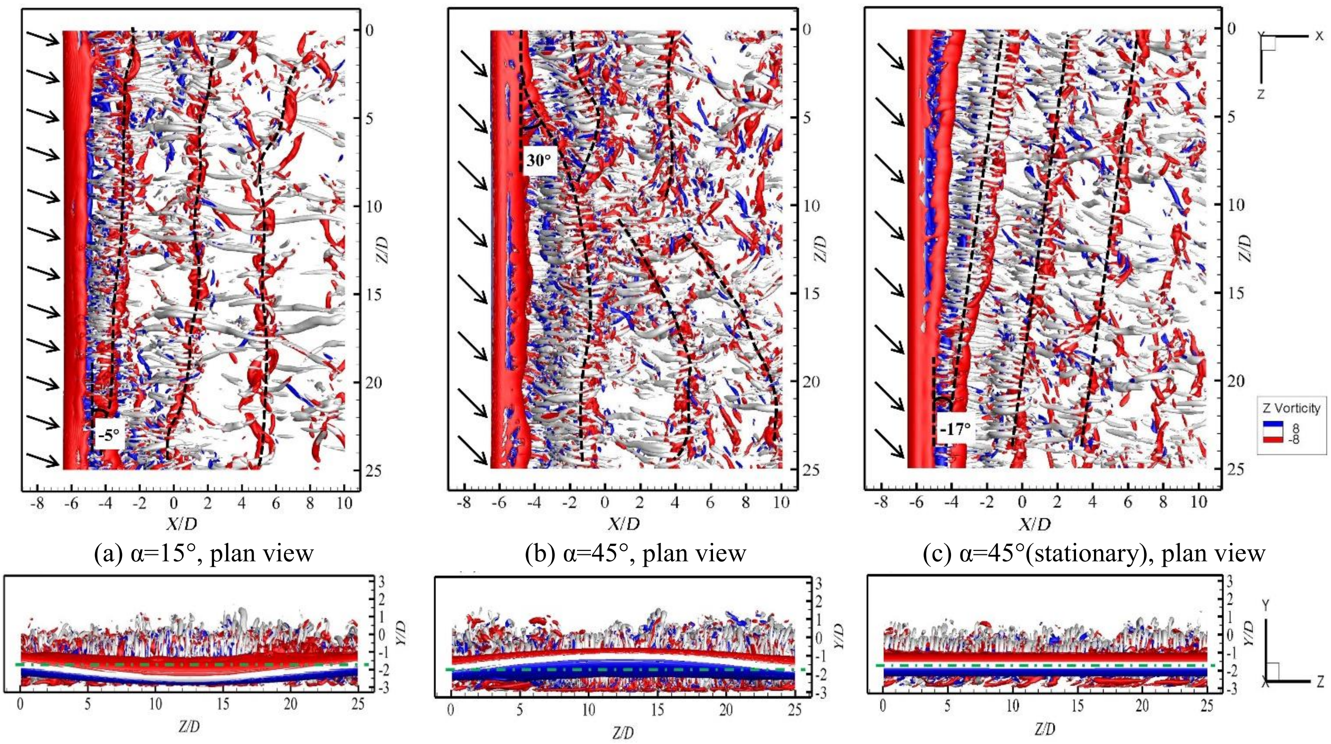

(a) α=15°, plan view (b) α=45°, plan view (c) α=45°(stationary), plan view

(d) α=15°, front view (e) α=45°, front view (f) α=45°(stationary), front view

Fig. 3 Instantaneous iso-surfaces of λ_2=-1.0 at α=15° and 45°, colored by the spanwise vorticity. The dashed black lines in (a - c) and the dashed-dotted green lines in (d - f) represent the spanwise vortex rows and the initial cylinder axis, respectively

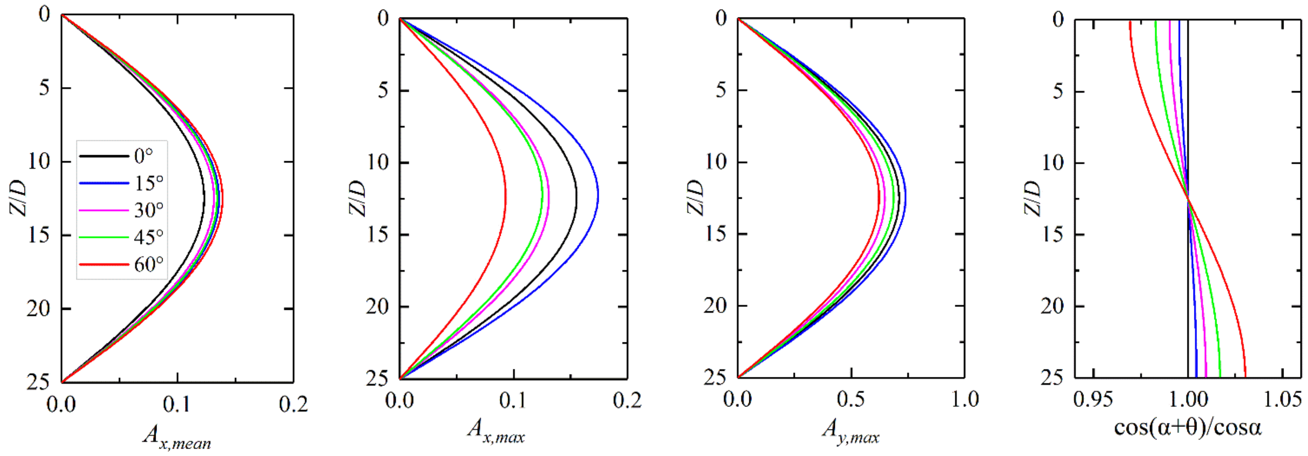

(a) Time-mean in-line displacement (b) Maximum in-line displacement (c) Maximum cross-flow displacement (d) Local normal inflow velocity

Fig. 4 Spanwise distributions of time-mean, maximum displacement and the local normal inflow velocity at different α. The local normal inflow velocity $U\cos(\alpha+\theta)$ in (d) is normalized by $U\cos\alpha$

3.2 Structural responses

The vibration responses of the flexible cylinder at different α are plotted in Figs. 4(a) - 4(c). As shown in Fig. 4(a), the maximum in-line bending of the cylinder is within 0.12 - 0.14*D*, and gradually increases with the increasing α, although the normal inflow velocity U_n is kept the same. As stated in Bourguet and Triantafyllou (2014), the in-line bending of the cylinder would change the local normal velocity $U\cos(\alpha+\theta)$ along the span, which would lead to a significant difference in the vibration responses between the inclined and normal cases. In the above, θ refers to the angle between the *z*-axis and the deformed cylinder axis, and it is positive when $0 < Z/D < 12.5$ and negative when $12.5 < Z/D < 25$. Fig. 4(d) shows the spanwise distribution of local normal velocity $U\cos(\alpha+\theta)$, normalized by U_n, at different α. The normalized local normal velocity profile at α = 60° shows significant variations along the span, from $\cos(\alpha+\theta)/\cos\alpha \approx 0.97$ ($Z/D = 0$) to 1.03 ($Z/D = 25$), despite the maximum θ is roughly 1° at the two ends of the cylinder. However, for α=0°, $\cos(\alpha+\theta)/\cos\alpha \approx 1.0$ along the span with a deviation smaller than 2×10^{-4}. That is, the local normal velocity at α = 0° is almost uniform along the span, whereas a non-uniform normal velocity profile which is analogous to a shear flow exists in the inclined cases due to the in-line bending of the cylinder. Moreover, the shear rate fastly increases with the increasing α, which is expected to have a significant influence on the flow-structure interactions.

The maximum vibration amplitudes in the in-line and cross-flow directions are symmetric about the midspan, irrespective of α (Figs. 4(b) - 4(c)). Due to the wall proximity, the in-line and cross-flow vibration wavenumbers are identical, which is different from the observation in the VIV of a wall-free flexible cylinder that a wavenumber ratio of 2 is established between the in-line and crossflow vibrations. The in-line vibration amplitude increases when α is increased from 0° to 15° but decreases with a further increase in α from 15°, being maximum at α = 15° (Fig. 4(b)). This is consistent with the nature of vortex shedding patterns, negatively- and positively-yawed vortex shedding patterns for α = 15° and ≥ 30°, respectively. The maximum in-line amplitude $A_{x,max}$ at the midspan is 13% larger than that at α=0°. However, $A_{x,max}$ decreases with further increasing α from 15°, being 40% smaller at α=60° than at α=0°, suggesting the violation of the IP. The crossflow amplitudes have a similar varying tendency with its in-line counterparts (Fig. 4(c)), but the difference between the yawed and normal cases is less than 12%. Therefore, it suggests that the yaw angle has more significant effects on the in-line vibrations than on the crossflow vibrations. Similar observation was also reported in the study of Bourguet and Triantafyllou (2014) that, for highly tensioned configurations, the crossflow vibration of a yawed (α ≠ 0°) cylinder is almost identical to that of a normal (α = 0°) cylinder, but the in-line vibrations exhibit obvious differences between the yawed and normal cases.

Due to the in-line bending of the cylinder, the local normal velocity $U\cos(\alpha+\theta)$ changes along the span, which may lead to asymmetric vibration responses of the cylinder. As shown in Fig. 4, the distributions of both in-line and cross-flow vibration amplitudes are symmetric about the midspan of the cylinder, regardless of α. However, the drag and lift coefficients do show asymmetric distributions in Fig. 5 when α is not zero. This is because the axial component of the flow is not much linked to in-line and cross-flow vibrations, at least to the first mode.

3.3 Hydrodynamic force coefficients

Fig. 5(a) shows the time-mean drag coefficient $\overline{C}_D$ along the span. It is seen that the $\overline{C}_D$ profile is generally symmetric about the midspan for α ≤ 15°, but exhibits obvious asymmetry at larger α, despite the in-line bending and the vibration responses of the cylinder are symmetric for all cases. Interestingly, at α ≥ 30° the $\overline{C}_D$ is larger at the upper half ($Z/D < 12.5$) than at the lower half ($Z/D > 12.5$) of the cylinder. Moreover, the maximum and span-averaged $\overline{C}_D$ generally

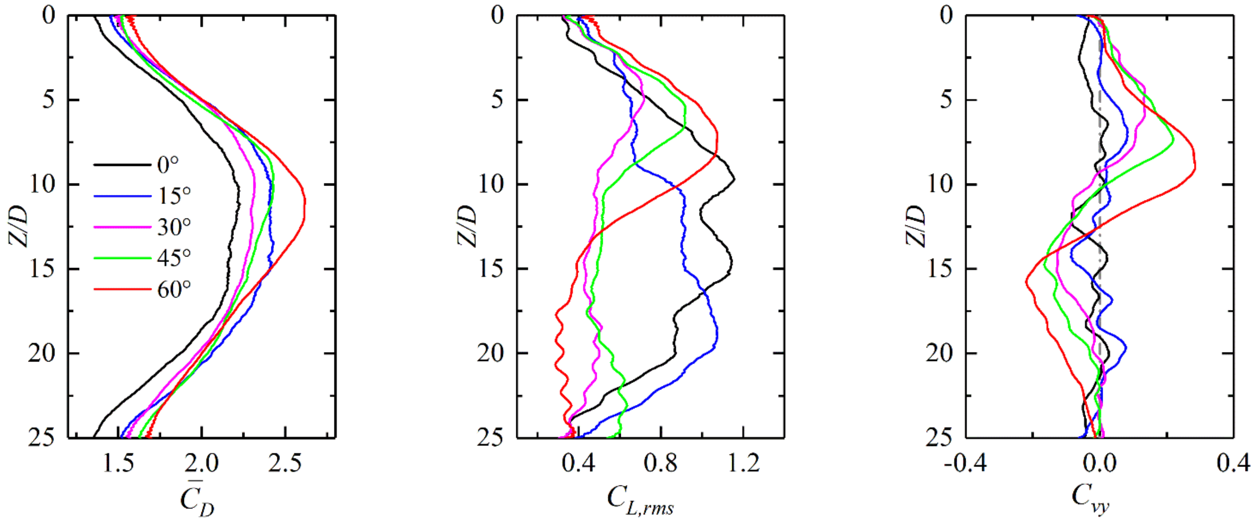

(a) Time-mean drag coefficient (b) RMS lift coefficient (c) Time-mean lift coefficient in phase with transverse vibration velocity

Fig. 5 Spanwise distributions of time-mean drag coefficient, RMS lift coefficient and time-mean lift coefficient in phase with transverse vibration velocity at different α.

grows when α is increased from 0° to 15° or 30° to 60°, with a drop between α = 15° and 30°. The span-averaged $\bar{C}_D$ is 1.89 for α = 0° and 2.11 for α = 60°, the difference being less than 12%.

Fig. 5(b) shows the spanwise distributions of the RMS lift coefficients $C_{L,rms}$. As expected, despite the significant fluctuations, the $C_{L,rms}$ distribution is generally symmetric about the midspan (Z/D = 12.5) for α = 0° but asymmetric for α ≠ 0°. The interesting point here is that the $C_{L,rms}$ for α = 15° is larger in the lower half span than in the upper half span (the dominant peak appearing on the lower half) while the correspondence between the $C_{L,rms}$ peak and half spans is opposite for α ≥ 30°, maximum $C_{L,rms}$ occurring in the upper side. It can be recalled that negatively-yawed vortex shedding was observed for α = 15° while positively-yawed vortex shedding prevailed for α ≥ 30°. This explains why $C_{L,rms}$ peak appears on the lower side for α=15° but on the upper side for α ≥ 30°.

As reported by Bourguet and Triantafyllou (2014), the vibration responses and fluid forces are closely related to the energy transfer between the fluid and the cylinder, and the transfer rate of energy can be quantified by the mean lift coefficient in phase with the transverse vibration velocity.

$$C_{vy} = \sqrt{2}\,\frac{\overline{C_L \dot{A}_y}}{\sqrt{\overline{\dot{A}_y^2}}} \tag{7}$$

where C_L refers to the instantaneous lift coefficient and $\dot{A}_y$ is the cross-flow velocities of the oscillating cylinder. Positive values of the C_{vy} indicate that the flow provides energy to excite the body oscillation, and the negative values mean that the structural vibrations are damped by the flow. The spanwise distributions of C_{vy} at different α are presented in Fig. 5(c). At α ≤ 15°, the C_{vy} fluctuates near zero, indicating the energy transferring is neutral. For α ≥ 30°, with an increase in α, the spanwise distribution of C_{vy} exhibits significant asymmetry by

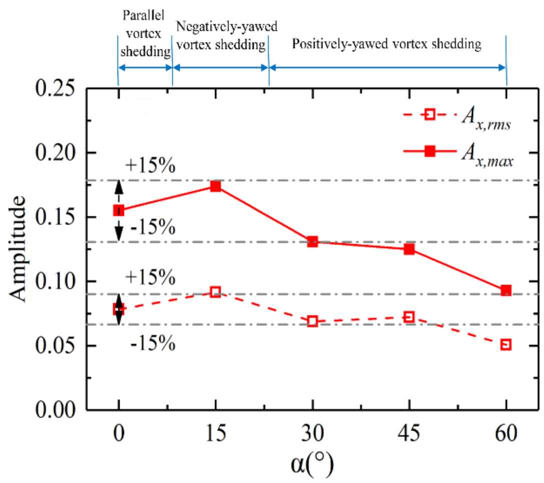

(a) Maximum and RMS of the in-line vibration amplitude

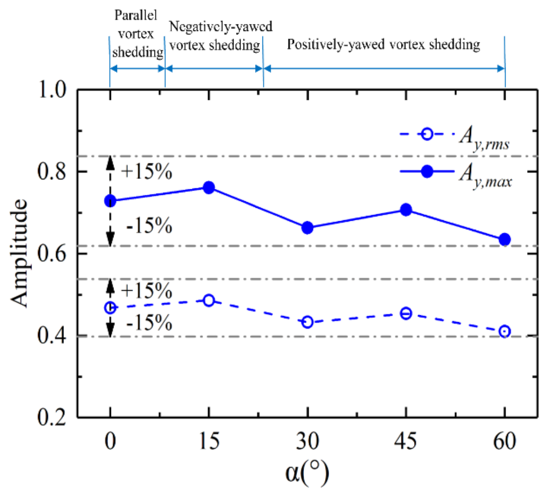

(b) Maximum and RMS of the cross-flow vibration amplitude

Fig. 6 Variations of the vibration amplitudes with α

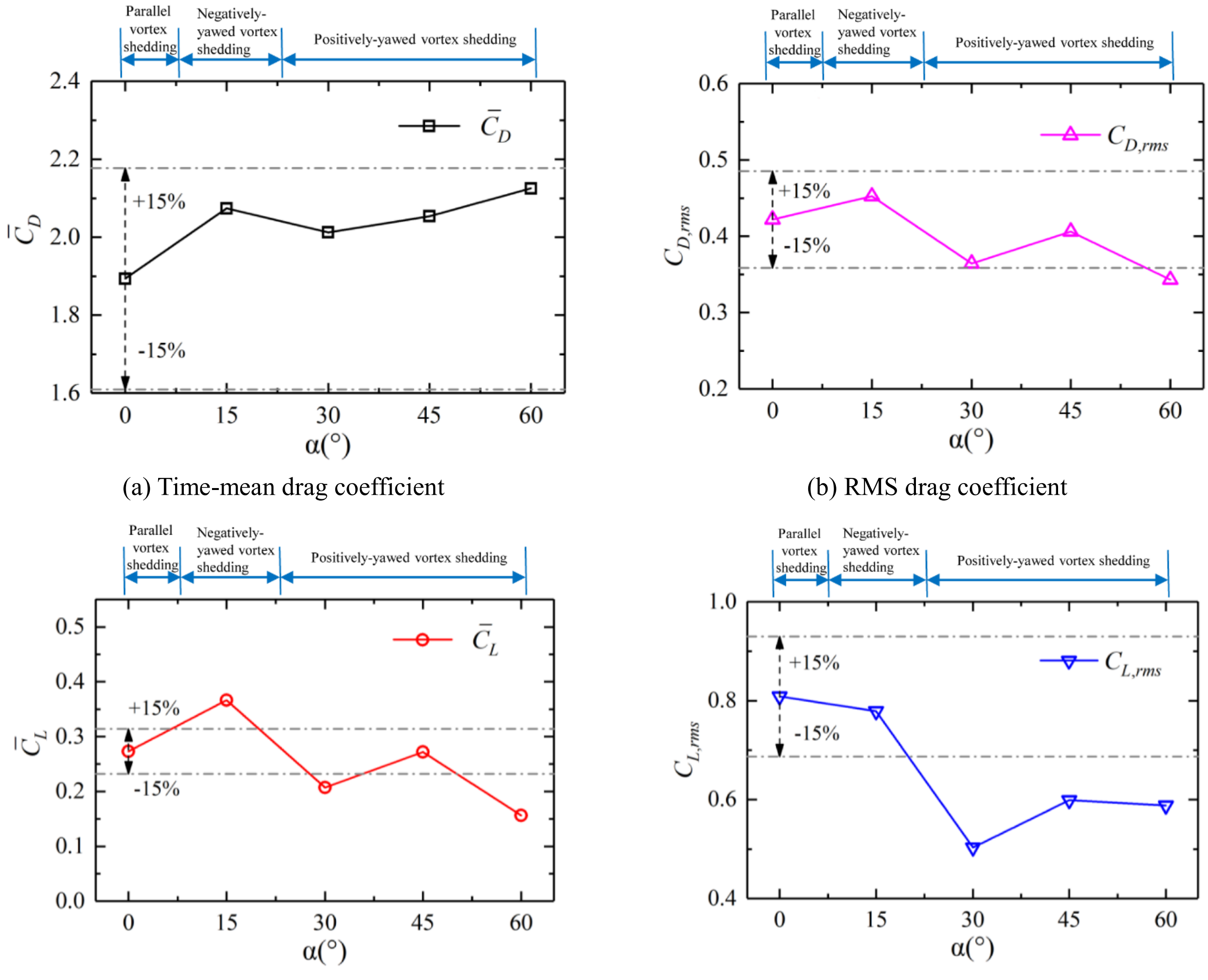

(a) Time-mean drag coefficient (b) RMS drag coefficient

(c) Time-mean lift coefficient (d) RMS lift coefficient

Fig. 7 Variations of the force coefficients with α

showing an increasing larger excitation region in the upper half and damping region in the lower half. This spatial distribution of C_{vy} indicates that energy is inputted into the vibrating cylinder at the upper half, then transferred to the lower half, and finally dissipated to the surrounding fluid at the lower half.

3.4 Independent principle

Fig. 6 shows the maximum and RMS of the in-line and cross-flow vibration amplitudes of the cylinder at the midspan (Z/D = 12.5). The corresponding shedding patterns are marked at the top of the figures. It is seen that the maximum ($A_{x,max}$) and RMS ($A_{x,rms}$) of the in-line vibration amplitude first increase and then decrease with the increment of α. Interestingly, the negatively-yawed vortex shedding results in the maximum $A_{x,max}$ and $A_{x,rms}$. Compared with the α = 0° case, the relative difference of $A_{x,max}$ at α = 15° is 13%, smaller than the criteria of 15% as suggested in Zhou *et al*. (2010), Franzini *et al*. (2013), Zhao *et al*. (2013). However, at larger α, the differences are 16% (α = 30°), 19% (α = 45°) and 40% (α = 60°), respectively, indicating the violation of the IP. For the $A_{x,rms}$, the differences between yawed and α = 0° cases are smaller than 15%, except for α=60° at which the IP fails to predict the in-line vibration responses. The IP is valid for predicting the in-line vibration upto α = 45°. As shown in Fig. 6(b), the maximum ($A_{y,max}$) and RMS ($A_{y,rms}$) of the cross-flow vibration amplitude both exhibit a first-increase-then-decrease trend, and the largest relative difference between α = 0° and α = 60° is less than 15%, which proves the validity of the IP in predicting the cross-flow vibration at α ≤ 60°.

Fig. 7 shows dependence on α of the span- and time-averaged hydrodynamic force coefficients. It is seen that the fluid forces on the vibrating cylinder are significantly larger than those on the stationary cylinder in Ji *et al*. (2019), which is also reported in Bourguet *et al*. (2015). The $\bar{C}_D$ at α ≠ 0° is larger than that at α = 0°, with a maximum increment of 12% at α = 60° (Fig. 7(a)). The RMS drag coefficient ($C_{D,rms}$) shows a similar trend to that of $A_{x,rms}$, with a difference larger than 15% at α = 60° (Fig. 7(b)). The time-mean lift coefficient ($\bar{C}_L$) exhibits large fluctuations with the increasing α, indicating a high sensitivity of the $\bar{C}_L$ on the flow conditions. The difference between the yawed and normal cases exceeds 15% for all α≠0° cases except α=45° (Fig. 7(c)). In Fig.7(d), a notable reduction in the RMS lift coefficient ($C_{L,rms}$) happens at α = 30°, corresponding to the change of the vortex-shedding

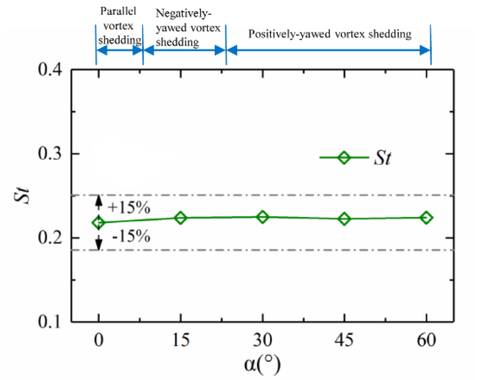

Fig. 8 Variations of the Strouhal number with α

pattern. The difference between α≠0° and α=0° cases violates the criteria when α ≥ 30°.

In Fig. 8, the Strouhal number (*St*) marginally increases with the increasing α while the maximum difference is smaller than 3% for all the yawed cases, proving the validity of the IP in the prediction of *St* at α ≤ 60°. Compared with the stationary case in Ji *et al*. (2019) in which the *St* increases with α and violates the criteria at α = 60°. The *St* is not much sensitive to α. This indicates that the vibrating cylinder has a more stable vortex-shedding frequency, thus a more stable vibrating frequency, due to the added mass effects.

4. Conclusions

Vortex-induced vibrations of a yawed flexible cylinder near a plane boundary are numerically investigated by using the immersed boundary method. The three-dimensional direct numerical simulations are carried out at Re_n = 500, G/D = 0.8 and α = 0°- 60°. The key conclusions are summarized as follows.

- Three distinct vortex shedding patterns are observed at different yaw angles, i.e., parallel vortex shedding (α = 0°), negatively-yawed vortex shedding (α = 15°) and positively-yawed vortex shedding (α ≥ 30°). However, the orientation of the spanwise vortex rows for α ≥ 30° is opposite to that for the stationary cylinder.
- Spanwise symmetry is observed in both in-line and cross-flow vibration amplitudes for all α examined. The difference of in-line amplitude between α≠0° and α=0° cases is larger than that of the cross-flow amplitude, indicating that the in-line vibrations are more sensitive to the yaw angle.
- The RMS lift coefficient $C_{L,rms}$ distribution is symmetric about the midspan for parallel vortex shedding (α = 0°) and asymmetric for α≠0°, with peaks in $C_{L,rms}$ occurring on the lower and upper sides for negatively- and positively-yawed vortex shedding patterns. Energy transfer between the flow and cylinder is neutral in the parallel vortex shedding, exhibiting increasingly larger in the exciting and damping regions for α ≠ 0°.
- The IP is valid in predicting the in-line vibration ($A_{x,rms}$) and hydroforces ($\overline{C}_D$ and $C_{D,rms}$) upto α=45°, and valid in predicting the cross-flow vibration ($A_{y,rms}$) at α ≤ 60°. However, the IP produces unacceptable errors in predicting the cross-flow hydroforces ($\overline{C}_L$, $C_{L,rms}$) at α ≥ 30°, due to the positively-yawed vortex shedding pattern.

Acknowledgments

This work was financially supported by the National Natural Science Foundation of China (Grants No. 51579175, 51779172 and 51979186), the Science Fund for Creative Research Groups of the National Natural Science Foundation of China (Grant No. 51621092). The National Key Research and Development Program of China (Grant No. 2017YFC1404200). The work was carried out at National Supercomputer Center in Tianjin, and the calculations were performed in Tianhe 3 prototype.

References

Alam, M.M. and Zhou, Y. (2007). “The turbulent wake of an inclined cylinder with water running”, *J. Flu. Mech*., **589**, 261-303. https://doi.org/10.1017/S0022112007007720.

Bai, H.L. and Alam, M.M. (2018), “Dependence of square cylinder wake on Reynolds Number”, *Phys. Flu.*, **30**, 015102. https://doi.org/10.1063/1.4996945.

Bearman, P.W. and Zdravkovich, M.M. (1978), “Flow around a circular cylinder near a plane boundary”, *J. Flu. Mech*., **89**(1), 33-47. https://doi.org/10.1017/S002211207800244X.

Bourguet, R. and Triantafyllou, M.S. (2014), “Vortex-induced vibrations of a flexible cylinder at large inclination angle”, *Philos. T. R. Soc. A. Math. Phys. Eng. Sci*., **373**(2033), 20140108-20140108. https://doi.org/10.1098/rsta.2014.0108.

Bourguet, Rémi, Em Karniadakis, G. and Triantafyllou, M.S. (2015), “On the validity of the independence principle applied to the vortex-induced vibrations of a flexible cylinder inclined at 60°”, *J. Flu. Struct*., **53**, 58-69. https://doi.org/10.1016/j.jfluidstructs.2014.09.005

Chen, W., Ji, C., Xu, D. and Srinil, N. (2019a), “Wake patterns of freely vibrating side-by-side circular cylinders in laminar flows”, *J. Flu. Struct*., **89**, 82-95. https://doi.org/10.1016/j.jfluidstructs.2019.02.013

Chen, W., Ji, C., Xu, D. and Williams, J. (2019b), “Two-degree-of-freedom vortex-induced vibrations of a circular cylinder in the vicinity of a stationary wall”, *J. Flu. Struct*., **91**, 102728. https://doi.org/10.1016/j.jfluidstructs.2019.102728

Derakhshandeh, J.F. and Alam, M.M. (2018), “Flow structures around a rectangular cylinder in the vicinity of a wall”, *Wind Struct*., **26**(5), 293-304.

Derakhshandeh, J.F. and Alam, M.M. (2019a), “A numerical study of heat transfer enhancement by a rectangular cylinder placed parallel to heated wall”, *J. Heat Transfer*, **141**, 071901.

Derakhshandeh, J.F. and Alam, M.M. (2019b), “A review of bluff body wakes”, *Ocean Eng*., **182**(15), 475-488. https://doi.org/10.1016/j.oceaneng.2019.04.093.

Franzini, G.R., GoncAlves, R.T., Meneghini, J.R. and Fujarra, A. L.C. (2013), “One and two degrees-of-freedom vortex-induced vibration experiments with yawed cylinders”, *J. Flu. Struct*., **42**, 401-420. https://doi.org/10.1016/j.jfluidstructs.2013.07.006.

Han, Q., Ma, Y., Xu, W., Lu, Y. and Cheng, A. (2017), “Dynamic characteristics of an inclined flexible cylinder undergoing vortex-induced vibrations”, *J. Sound Vib*., **394**, 306-320. https://doi.org/10.1016/j.jsv.2017.01.034.

He, G.S., Wang, J.J., Pan, C., Feng, L.H., Gao, Q. and Rinoshika,

A. (2017), "Vortex dynamics for flow over a circular cylinder in proximity to a wall", *J. Flu. Mech*., **812**, 698-720. https://doi.org/10.1016/j.jfluidstructs.2013.07.006.

Hsieh, S.C., Low, Y.M. and Chiew, Y.M. (2016), "Flow characteristics around a circular cylinder subjected to vortex-induced vibration near a plane boundary", *J. Flu. Struct*., **65**, 257-277. https://doi.org/10.1016/j.jfluidstructs.2016.06.007.

Jeong, J.J.J. and Hussain, F. (1995), "On the identification of a vortex", *J. Flu. Mech*., **332**(1), 339-363. https://doi.org/10.1017/S0022112095000462.

Ji, C., Cui, Y., Xu, D., Yang, X. and Srinil, N. (2019b), "Vortex-induced vibrations of dual-step cylinders with different diameter ratios in laminar flows", *Phys. Fluids*, **31**, 073602. https://doi.org/10.1063/1.5097730.

Ji, C., Munjiza, A. and Williams, J.J.R. (2012), "A novel iterative direct-forcing immersed boundary method and its finite volume applications", *J. Comput. Phys*., **231**(4), 1797-1821. https://doi.org/10.1016/j.jcp.2011.11.010.

Ji, C., Zhang, Z., Xu, D. and Srinil, N. (2019a), "Three-dimensional direct numerical simulations of flows past an inclined cylinder near a plane boundary", *Proceedings of the 38th International Conference on Ocean, Offshore and Arctic Engineering* (*OMAE2019*), Glasgow, Scotland. June.

Jiang, H. and Cheng, L. (2017), "Strouhal–Reynolds number relationship for flow past a circular cylinder", *J. Flu. Mech*., **832**, 170-188. https://doi.org/10.1017/jfm.2017.685.

Lei, C., Cheng, L. and Kavanagh, K. (1999), "Re-examination of the effect of a plane boundary on force and vortex shedding of a circular cylinder", *J. Wind Eng. Ind. Aerod*., **80**(3), 263-286. https://doi.org/10.1016/S0167-6105(98)00204-9.

Lei, C., Cheng, L., Armfield, S.W. and Kavanagh, K. (2000), "Vortex shedding suppression for flow over a circular cylinder near a plane boundary", *Ocean Eng*., **27**(10), 1109-1127. https://doi.org/10.1016/S0029-8018(99)00033-5.

Li, Z., Yao, W., Yang, K., Jaiman, R.K. and Khoo, B.C. (2016), "On the vortex-induced oscillations of a freely vibrating cylinder in the vicinity of a stationary plane wall", *J. Flu. Struct*., **65**, 495-526. https://doi.org/10.1016/j.jfluidstructs.2016.07.001.

Mansy, H., Yang, P. and Williams D.R. (1994), "Quantitative measurements of spanwise-periodic three-dimensional structures in the wake of a circular cylinder", *J. Fluid Mech*. **270**, 277-296. https://doi.org/10.1017/S0022112094004271.

Mittal, R. and Balachandar, S. (1995), "Effect of three-dimensionality on the lift and drag of nominally two-dimensional cylinders. *Phys. Flu*., **7**(8), 1841. https://doi.org/10.1063/1.868500

Peskin, C.S. (1972), "Flow patterns around heart valves: a numerical method", *J. Comput. Phys*., **10**(2), 252-271. https://doi.org/10.1016/0021-9991(72)90065-4

Ramberg, S.E. (2006), "The effects of yaw and finite length upon the vortex wakes of stationary and vibrating circular cylinders", *J. Flu. Mech*., **128**(128), 81-107. https://doi.org/10.1017/S0022112083000397

Sarkar, S. and Sarkar, S. (2010), "Vortex dynamics of a cylinder wake in proximity to a wall", *J. Flu. Struct*., **26**(1), 19-40. https://doi.org/10.1016/j.jfluidstructs.2009.08.003

Tham, D. M. Y., Gurugubelli, P.S., Li, Z. and Jaiman, R.K. (2015), "Freely vibrating circular cylinder in the vicinity of a stationary wall", *J. Flu. Struct*., **59**, 103-128. https://doi.org/10.1016/j.jfluidstructs.2015.09.003

Thapa, J., Zhao, M., Zhou, T. and Cheng, L. (2014), "Three-dimensional simulation of vortex shedding flow in the wake of a yawed circular cylinder near a plane boundary at a Reynolds number of 500", *Ocean Eng*., **87**, 25-39. https://doi.org/10.1016/j.oceaneng.2014.05.014

Wang, X.K. and Tan, S.K. (2008), "Comparison of flow patterns in the near wake of a circular cylinder and a square cylinder placed near a plane wall", *Ocean Eng*., **35**(5-6), 458-472. https://doi.org/10.1016/j.oceaneng.2008.01.005.

Wang, X.K. and Tan, S.K. (2008), "Near-wake flow characteristics of a circular cylinder close to a wall", *J. Flu. Struct*., **24**(5), 605-627. https://doi.org/10.1016/j.jfluidstructs.2007.11.001.

Wang, X.K., Hao, Z. and Tan, S.K. (2013), "Vortex-induced vibrations of a neutrally buoyant circular cylinder near a plane wall", *J. Flu. Struct*., **39**, 188-204. https://doi.org/10.1016/j.jfluidstructs.2013.02.012.

Williamson, C.H.K. (1996), "Three-dimensional wake transition", *J. Flu. Mech*., **328**(10), 345-407. https://doi.org/10.1017/S0022112096008750.

Williamson, C.H.K. (2003), "Vortex dynamics in the cylinder wake", *Annu. Rev. Flu. Mech.*, **28**(1), 477-539. https://doi.org/10.1146/annurev.fl.28.010196.002401.

Williamson, C.H.K. and Roshko, A. (1990), "Measurements of base pressure in the wake of a cylinder at low Reynolds numbers", *Zeitschrift für Flugwissenschaften und Weltraumforschung*, **14**(1), 38-46. https://doi.org/ 10.2514/3.55610.

Wu, J., Sheridan, J., Soria, J. and Welsh, M.C. (1994), "An experimental investigation of streamwise vortices in the wake of a bluff body", *J. Flu. Struct*., **8**(7), 621-635. https://doi.org/10.1006/jfls.1994.1031.

Xu, W., Ma, Y., Ji, C. and Sun, C. (2018), "Laboratory measurements of vortex-induced vibrations of a yawed flexible cylinder at different yaw angles", *Ocean Eng*., **154**, 27-42. https://doi.org/10.1016/j.oceaneng.2018.01.113.

Yoon, H.S., Lee, J.B., Seo, J.H. and Park, H.S. (2010), "Characteristics for flow and heat transfer around a circular cylinder near a moving wall in wide range of low Reynolds number", *Int. J. Heat Mass Transfer*, **53**(23-24), 5111-5120. https://doi.org/10.1016/j.ijheatmasstransfer.2010.07.054.

Younis, M.Y., Alam, M.M. and Zhou, Y. (2016), "Flow around two nonparallel tandem cylinders", *Phys. Flu*., **28**, 125106. https://doi.org/10.1063/1.4972549.

Zang, Z. and Zhou, T. (2017), "Transverse vortex-induced vibrations of a near-wall cylinder under oblique flows", *J. Flu. Struct*., **68**, 370-389. https://doi.org/10.1016/j.jfluidstructs.2016.11.021.

Zhao, M., Cheng, L. and Zhou, T. (2009), "Direct numerical simulation of three-dimensional flow past a yawed circular cylinder of infinite length", *J. Flu. Struct*., **25**(5), 831-847. https://doi.org/10.1016/j.jfluidstructs.2009.02.004.

Zhao, M., Thapa, J., Cheng, L. and Zhou, T. (2013), "Three-dimensional transition of vortex shedding flow around a circular cylinder at right and oblique attacks", *Phys. Flu*., **25**(1), 014105. https://doi.org/10.1063/1.4788934.

Zhou, T., Wang, H., Razali, S.F.M., Zhou, Y. and Cheng, L. (2010), "Three-dimensional vorticity measurements in the wake of a yawed circular cylinder", *Phys. Flu*., **22**(1), 015108. https://doi.org/10.1063/1.3291072.

AM